

Directional light emission enhancement from LED-phosphor converters using dielectric Vogel spiral arrays

Cite as: APL Photonics **3**, 126103 (2018); <https://doi.org/10.1063/1.5052637>

Submitted: 20 August 2018 . Accepted: 31 October 2018 . Published Online: 04 December 2018

Sean Gorsky, Ran Zhang, Abdullah Gok, Ren Wang, Kidanemariam Kebede,  Alan Lenef, Madis Raukas, Luca Dal Negro, et al.

COLLECTIONS

 This paper was selected as an Editor's Pick



[View Online](#)



[Export Citation](#)



[CrossMark](#)

ARTICLES YOU MAY BE INTERESTED IN

Engineered hyperuniformity for directional light extraction

APL Photonics **4**, 110801 (2019); <https://doi.org/10.1063/1.5124302>

Enhanced photoluminescence and directional white-light generation by plasmonic array

Journal of Applied Physics **124**, 213105 (2018); <https://doi.org/10.1063/1.5050993>

Inhibition of tunneling and edge state control in polariton topological insulators

APL Photonics **3**, 120801 (2018); <https://doi.org/10.1063/1.5043486>



THE ADVANCED MATERIALS MANUFACTURER®

sapphire windows Nd:YAG

spintronics raman substrates

silver nanoparticles perovskites

MOCVD beta-barium borate

rare earth metals quantum dots

osmium scintillation Ce:YAG

refractory metals laser crystals

anode lithium niobate InAs wafers

dysprosium pellets MOFs AuNPs

chalcogenides ZnS CdTe

perovskite crystals transparent ceramics

yttrium iron garnet

glassy carbon

beamsplitters

fused quartz

additive manufacturing

organometallics

transparent ceramics

CIGS

cermets

nanodispersions

MBE grade materials

thin film

OLED lighting

solar energy

sputtering targets

fiber optics

h-BN deposition slugs

CVD precursors

photovoltaics

metamaterials

borsosilicate glass

YBCO superconductors

InGaAs

indium tin oxide

MgF₂ rutile

diamond micropowder

optical glass

zeolites III-V semiconductors

barium fluoride

europtium phosphors

photronics

infrared dyes

surface functionalized nanoparticles

cerium oxide polishing powder

europium phosphors

transparent ceramics

CIGS

Al Sb P S Cl Ar

MBE grade materials

cermet

nanodispersions

thin film

Ga As Se Br Kr

OLED lighting

translucent

targets

solar energy

Tl Pb Bi Po At Rn

h-BN deposition

slugs

fiber optics

targets

Ts Og

CVD precursors

photovoltaics

metamaterials

borosilicate glass

Yttria Barium Zinc

europium phosphors

transparent

ceramics

CIGS

Al Sb P S Cl Ar

MBE grade materials

cermet

nanodispersions

thin film

Ga As Se Br Kr

OLED lighting

translucent

targets

solar energy

Tl Pb Bi Po At Rn

h-BN deposition

slugs

fiber optics

targets

Ts Og

CVD precursors

photovoltaics

metamaterials

borosilicate glass

Yttria Barium Zinc

europium phosphors

transparent

ceramics

CIGS

Al Sb P S Cl Ar

MBE grade materials

cermet

nanodispersions

thin film

Ga As Se Br Kr

OLED lighting

translucent

targets

solar energy

Tl Pb Bi Po At Rn

h-BN deposition

slugs

fiber optics

targets

Ts Og

CVD precursors

photovoltaics

metamaterials

borosilicate glass

Yttria Barium Zinc

europium phosphors

transparent

ceramics

CIGS

Al Sb P S Cl Ar

MBE grade materials

cermet

nanodispersions

thin film

Ga As Se Br Kr

OLED lighting

translucent

targets

solar energy

Tl Pb Bi Po At Rn

h-BN deposition

slugs

fiber optics

targets

Ts Og

CVD precursors

photovoltaics

metamaterials

borosilicate glass

Yttria Barium Zinc

europium phosphors

transparent

ceramics

CIGS

Al Sb P S Cl Ar

MBE grade materials

cermet

nanodispersions

thin film

Ga As Se Br Kr

OLED lighting

translucent

targets

solar energy

Tl Pb Bi Po At Rn

h-BN deposition

slugs

fiber optics

targets

Ts Og

CVD precursors

photovoltaics

metamaterials

borosilicate glass

Yttria Barium Zinc

europium phosphors

transparent

ceramics

CIGS

Al Sb P S Cl Ar

MBE grade materials

cermet

nanodispersions

thin film

Ga As Se Br Kr

OLED lighting

translucent

targets

solar energy

Tl Pb Bi Po At Rn

h-BN deposition

slugs

fiber optics

targets

Ts Og

CVD precursors

photovoltaics

metamaterials

borosilicate glass

Yttria Barium Zinc

europium phosphors

transparent

ceramics

CIGS

Al Sb P S Cl Ar

MBE grade materials

cermet

nanodispersions

thin film

Ga As Se Br Kr

OLED lighting

translucent

targets

solar energy

Tl Pb Bi Po At Rn

h-BN deposition

slugs

fiber optics

targets

Ts Og

CVD precursors

photovoltaics

metamaterials

borosilicate glass

Yttria Barium Zinc

europium phosphors

transparent

ceramics

CIGS

Al Sb P S Cl Ar

MBE grade materials

cermet

nanodispersions

thin film

Ga As Se Br Kr

OLED lighting

translucent

targets

solar energy

Tl Pb Bi Po At Rn

h-BN deposition

slugs

fiber optics

targets

Ts Og

CVD precursors

photovoltaics

metamaterials

borosilicate glass

Yttria Barium Zinc

europium phosphors

transparent

ceramics

CIGS

Al Sb P S Cl Ar

MBE grade materials

cermet

nanodispersions

thin film

Ga As Se Br Kr

OLED lighting

translucent

targets

solar energy

Tl Pb Bi Po At Rn

h-BN deposition

slugs

fiber optics

targets

Ts Og

Directional light emission enhancement from LED-phosphor converters using dielectric Vogel spiral arrays

Sean Gorsky,¹ Ran Zhang,¹ Abdullah Gok,¹ Ren Wang,¹ Kidanemariam Kebede,¹ Alan Lenef,² Madis Raukas,² and Luca Dal Negro^{1,3,4,a}

¹*Department of Electrical and Computer Engineering, Boston University, Boston, Massachusetts 02215, USA*

²*CTO Materials, OSRAM Opto Semiconductors, Beverly, Massachusetts 01915, USA*

³*Division of Materials Science and Engineering, Boston University, Boston, Massachusetts 02446, USA*

⁴*Department of Physics, Boston University, Boston, Massachusetts 02215, USA*

(Received 20 August 2018; accepted 31 October 2018; published online 4 December 2018)

Increasing light extraction efficiency and narrowing the angular spread of light emitted from optically thick light emitting diodes (LEDs) are desirable but difficult goals to achieve. In this paper, we design, optimize, and fabricate Vogel spiral arrays of dielectric nanostructures for optical directional extraction enhancement of incoherent emission from optically thick phosphor-converted LEDs. In order to design and optimize large-scale structures, we perform a systematic numerical investigation based on full-vector three-dimensional finite difference time domain simulations using a cloud of randomly positioned and randomly phased dipoles that approximate an incoherent Lambertian source. An analytical model based on kinematic scattering is also developed and used to parametrically study changes in the emission profile as the spiral geometry is tuned. The optimal Vogel spiral arrays are fabricated as TiO₂ nanodisks atop YAG:Ce³⁺ blue-to-white converter layers using electron-beam lithography and reactive ion etching. Photoluminescence spectroscopy is used to experimentally measure extraction enhancement up to 2× compared to a flat reference. Finally, accurate Fourier-space (k-space) fluorescence spectroscopy is used to measure the emission intensity profile up to 54° in a single snapshot image, and we find up to a 35% enhancement in power-normalized forward emission compared to a flat reference, under remote laser excitation. The integration of optimized Vogel spiral arrays of dielectric nanoparticles with phosphor-converted LEDs will increase efficiency and narrow the directional spread of light. These effects are beneficial to a variety of active device applications, including imaging, lighting, and projecting devices that require enhanced extraction efficiency combined with directional emission. © 2018 Author(s). All article content, except where otherwise noted, is licensed under a Creative Commons Attribution (CC BY) license (<http://creativecommons.org/licenses/by/4.0/>). <https://doi.org/10.1063/1.5052637>

I. INTRODUCTION

Commercial applications such as display, projection, and illumination devices stimulate the research on high-brightness, highly directional, and highly efficient light emitters.^{1–6} Modern semiconductor based light emitting diodes (LEDs) have almost ideal internal emission properties (almost 100% internal quantum efficiency)^{7,8} and have simple, durable, and robust structures. These properties make them a favorite candidate to the various optical applications. However, not all light generated within the LED is able to escape into free space due to total internal reflection (TIR) at

^adalnegro@bu.edu

the LED-air interface. Indeed, the light extraction efficiency is a significant limiter in the overall wall-plug efficiency of modern LEDs.⁹ Furthermore, isotropic emission within optically thick LEDs and flat interfaces results in nearly Lambertian radiant intensity, whereas narrower emission without reduction in emitted power would be beneficial for commercial applications.^{6,10}

A typical approach to improve the extraction efficiency and shape the emission is by patterning the surface of the semiconductor LEDs with periodic photonic crystals.^{11–19} A fraction of the light that reaches the interface at angles larger than the critical angle can be extracted through momentum matching in k-space.²⁰ However, the discrete nature of the reciprocal space of periodic photonic crystals limits the domain of extractable wave vectors. Alternative designs such as surface roughening,^{21,22} angle tilting,²³ and multi-facet usage of LEDs²⁴ also yield an increase in the extraction efficiency but at the expense of difficulty in design control, fabrication, or an increase in étendue.²² Recently, deterministic aperiodic arrays with diffuse and isotropic Fourier space have been proposed as a versatile approach to radiation engineering in aperiodic reciprocal space.²⁵ Moreover, it has been demonstrated that for low refractive index contrast, structures with isotropic k-space lead to omnidirectional scattering.^{14,25} These structures, when integrated with thin-film active waveguide-coupled LEDs, resulted in enhanced light extraction with controllable directional emission.^{26,27} For instance, it was recently shown that the small number of modes supported by thin-layer waveguide-coupled LED enable simple design rules that leverage the denser and more isotropic Fourier space of Vogel spirals to achieve broadband momentum matching. In particular, the golden angle (GA) Vogel spiral is a deterministic pattern which has isotropic light scattering properties.^{28,29} However, many commercial LED applications do not make use of thin-layer waveguide-coupled geometries but rely instead on optically thick emitting materials that produce partially coherent radiation with angularly broad emission characteristics approximated by a Lambertian source. Therefore, there is currently a compelling need to develop alternative approaches that enhance the extraction efficiency while simultaneously achieving better directionality of the angular emission in optically thick, partially incoherent LEDs. The engineering of directional emission of partially coherent radiation is a very challenging task that requires the development of a comprehensive modeling strategy beyond the traditional approaches of plane waves transmission and single dipole excitations.^{30,31}

In this work, we demonstrate enhanced light extraction and directional control using engineered Vogel spiral arrays of dielectric nanoparticles on top of an optically thick LED active material. Coordinates (r, θ) of a Vogel spiral array are generated using the simple rules,^{28,32,33}

$$r_n = a\sqrt{n}, \quad (1)$$

$$\theta_n = n\alpha, \quad (2)$$

where $n = 0, 1, 2, \dots$ is an integer and a and α are constants. For this research, we use the GA Vogel spiral array which has $\alpha \approx 137.508^\circ$ and has mean particle separation $\langle r \rangle = 1.7a$. The isotropic Fourier space and deterministic nature of this pattern makes it ideal for engineering directional light extraction from LEDs. Numerical Finite Difference Time Domain (FDTD) simulations in three spatial dimensions (3D) are performed using an incoherent ensemble of 45 excitation dipoles with random position, orientation, and phase to model isotropic emission within the active LED material and yield approximately Lambertian emission characteristics of optically thick LED materials. Numerical simulations predict a theoretical maximum extraction enhancement of $2.7\times$ when compared to a flat reference. An analytical model is also developed which allows for expedient prediction of the emission profile for a given spiral geometry. The optimal Vogel spiral arrays for extraction and directional emission enhancement are then fabricated by forming TiO₂ nanodisks atop a YAG:Ce³⁺ ceramic material layer (hereto referred to as a “converter layer”) using electron-beam lithography and reactive ion etching. Using photoluminescence (PL) spectroscopy, we measure extraction enhancement up to $2\times$ compared to a flat reference. We also use accurate Fourier space (k-space) fluorescence spectroscopy^{26,34} to measure the full emission profile up to a microscope objective limited 54° in a single snapshot and find up to 35% enhancement in power-normalized forward emission enhancement compared to a planar LED. The measured extraction enhancement and power-normalized directional enhancement are both found to be in good agreement with the results from the kinematic scattering model and

FDTD simulations. These results suggest that fabricating optimized Vogel spiral arrays of dielectric nanoparticles on top of active LED materials is beneficial to the wide variety of active device applications which required increased extraction efficiency and directional control of the emitted light.

II. FDTD SIMULATION

Lambertian emission of light from LED surfaces results from incoherent and isotropic emission within the converter layer. In order to simulate Lambertian emission, we incoherently average the results of ten different simulations where each simulation consists of 45 randomly located, oriented, and phased dipoles within the converter layer. A minimum separation of 500 nm between dipoles is enforced to avoid dipole coupling. This technique produces isotropic radiation within the high index medium and results in a nearly Lambertian surface emission profile.

The converter layer is rectangular with a length and width of 20 μm each, a depth of 6 μm , and an index of refraction $n = 1.82$ ($k = 0$). The simulation window is bound tightly to the sides of the converter layer with a 2 μm air gap above the top. The dipole sources are placed within the top 3 μm of the converter layer below the air gap with a vertical perfect electric conductor (PEC) boundary surrounding them to prevent horizontal radiation emission. The PEC boundary is separated from the simulation boundary by 500 nm on all sides. All boundaries of the simulation windows are set as perfectly matched layers (PMLs) to prevent radiation from reflecting back into the converter. TiO_2 disks are arranged in a GA Vogel spiral array atop the converter (see Fig. 4 for measured dispersion data). The disks have height H , mean separation $\langle r \rangle$, and diameter D , and are located at positions according to Eq. (1). The monitor is located 1 μm above the disks, and the far-field intensity in k-space is calculated. Optimization is performed by parametrically studying power extracted from the converter surface as the geometric parameters are tuned. Extraction enhancement is estimated by dividing power extracted from a patterned surface by the power extracted from a flat surface. All simulations are performed with free space wavelength $\lambda = 550$ nm.

We note that the efficiency measurements presented in this work cannot be compared directly with a fully packaged LED device. This research is in fact performed with a conversion platelet with all planar surfaces except the one which is patterned and is externally pumped with a blue laser. On the other hand, commercially packaged LEDs have many additional components surrounding the conversion phosphor, for example, the pump is typically a blue quantum dot emitter glued to the bottom and there may be reflectors on the sides and bottom. These additional elements may affect the internal radiation profile which will in turn modify the emission profile and the extracted power through the top surface. However, these configuration-dependent features are beyond the scope of this paper whose aim is to investigate the interaction between the nanostructured surface and the isotropic internal radiation profile incident at the surface of the device using a flat surface as a baseline measurement. This approach enables unambiguous quantitative comparisons with the published literature on textured surfaces for extraction enhancement^{35–37}

Figure 1(a) shows extraction enhancement as a function of $D/\langle r \rangle$ for four different H values. The shape of the enhancement curve is independent of H and always has a peak value at $D/\langle r \rangle = 0.6$, and peak enhancement occurs for $H = 300$ nm. Figure 1(b) gives enhancement as a function of $D/\langle r \rangle$ for various D . The shape is again largely insensitive to D with peak always occurring around $D/\langle r \rangle = 0.6$. Maximum enhancement of 2.7× occurs for $H = 300$ nm, $D = 130$ nm, and $\langle r \rangle = 220$ nm. The k-space intensity distribution from four different spirals and a flat reference are shown in Fig. 1(c). These curves are the azimuthally averaged far-field intensity in k-space divided by total emitted power. In the x-axis, β' is the transverse component of the free space wave vector. The flat surface simulation shows approximately Lambertian emission (black solid line) up to $\beta'/k_o \approx 0.9$ ($\sin^{-1}(0.9) = 64^\circ$), where it suddenly drops to zero. Figure 1(d) shows the power-normalized directional enhancement, γ_{dn} , calculated by dividing the flat reference curve with respect to the patterned curves. This metric shows the redistribution of power in k-space and is insensitive to the total extraction enhancement. For $\langle r \rangle = 220, 340$ and 680 nm, the emission profile is nearly identical, with peak enhancement in the forward direction of 1.4×. For $\langle r \rangle = 510$ nm, the peak enhancement is reduced to 1.2×. The shape and magnitude of these curves are in good agreement with measurements

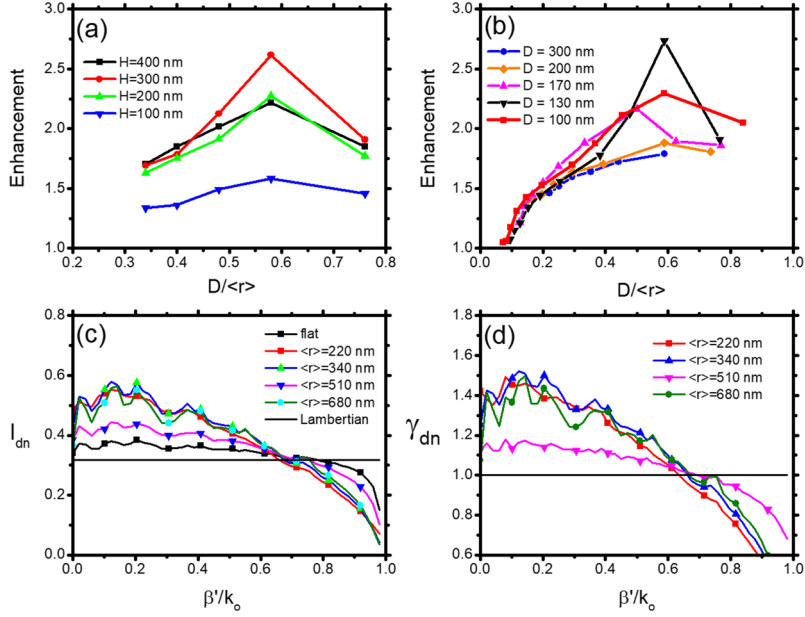


FIG. 1. (a) Extraction enhancement vs. spiral geometry for four different pillar heights. Peak value for all cases occurs at $D/\langle r \rangle = 0.6$, and the optimal pillar height is $H = 300$ nm. (b) Extraction enhancement vs. spiral geometry for various D . Peak values consistently occur around $D/\langle r \rangle = 0.6$ with a peak for $D = 130$ nm ($\langle r \rangle = 215$ nm). (c) Power-normalized angular intensity in k-space, where β' is the transverse component of the free space wave vector. The black solid line is a Lambertian source, and the black line with squares is a flat surface simulation which yields an approximately Lambertian emission profile. (d) Power-normalized directional enhancement shows enhanced forward emission for all cases, but there is no clear trend as $\langle r \rangle$ varies.

later shown Fig. 7. In Sec. III, we develop an analytical model to qualitatively predict the intensity profile for a given particle array. This model gives a deeper understanding into how the scattering particles enable light extraction enhancement and why GA Vogel spirals are well suited for the task. Additionally, this model provides a means to more efficiently assess and compare different particle arrays.

III. ANALYTICAL MODEL

The ability to perform systematic studies using 3D-FDTD simulations is limited by the amount of time and computational resources needed to deal with heterogeneous systems whose dimensions are much larger than the wavelength. This is especially true for the simulation of aperiodic arrays, where it is necessary to simulate a large number of particles without the convenience of periodic boundary conditions allowed by periodic photonic crystals. Furthermore, while numerical simulation yields quantitative results, it is often difficult to extract a genuine understanding of the physical interaction which is valuable for engineering application. In this section, we discuss the development and application of a kinematic scattering model which qualitatively predicts the LED emission profile for a given particle array atop a thick incoherent emitter. Using this model, we perform a parametric study of the emission profile as the mean particle separation of the GA Vogel spiral array is changed. The results are shown to be in good qualitative agreement with both the FDTD predictions and the measurements discussed in Sec. V.

Extraction efficiency in optically thick planar LEDs is limited by TIR. For example, with an isotropically emitting source embedded in a material with refractive index n , the fraction of light extracted from a single surface is given by $\eta_{extr} = \int_0^{\theta_c} \sin(\theta) d\theta = \frac{1}{2}[1 - \cos(\theta_c)]$. For YAG:Ce³⁺, $n = 1.82$ for which $\theta_c = 33^\circ$ and $\eta_{extr} = 8.1\%$. Assuming there are reflective boundaries on the other five surfaces, and neglecting absorption and re-emission or other methods for redistributing the light, the remaining light is guided within the medium and is unable to escape.

Nanoparticles on top of the emitting surface act collectively as a diffracting element which can scatter TIR light into free space. This effect has been shown to both increase extraction efficiency and shape the emitted radiation in optically thin LEDs.⁹ Shaping the emission can also be achieved by forming a photonic crystals from the converter itself, thereby inhibiting emission at TIR angles, but this is a distinct effect from the one considered in this work.^{20,38}

We model the interaction between upward propagating light and the particle array using Bragg's law of diffraction. This method for predicting emission profiles has been successfully applied to model the emission profile from a thin active layer which acts as a waveguide and thus only allows a discrete set of wave vectors to propagate within.^{9,26} Here we modify the approach and make it applicable to a thick active layer where an angular continuum of waves are able to propagate.

Figure 2 shows the geometry under consideration. A plane wave with wave vector $k_o = 2\pi/\lambda$ incident on a high-to-low index boundary with transverse wave vector β will undergo TIR if its transverse momentum is outside the free-space light cone, $|\beta| > k_o$. If a particle array is present on the surface then the incident wave can interact with the lattice momentum vector G , and if the total transverse momentum $|\beta + G| < k_o$ then a portion of the wave will scatter into free space with transverse direction $\beta' = \beta + G$. The coupling strength, or the fraction of the incident wave that scatters into free space, is given by the spatial power spectral density of the array, which in the present case consists of circular pillars of diameter D located at points r_i arranged in a GA Vogel spiral array according to Eq. (1). The coupling strength can thus be written as

$$S(G) = \frac{\pi D}{N} \left| \frac{J_1(DG/2)}{G} \sum_{i=1}^N e^{jG \cdot r_i} \right|^2, \quad (3)$$

where the Airy function, $(\pi D/G) J_1(DG/2)$, accounts for diffraction by a single disk and the summation accounts for the array of the disks.

Let $I_{in}(\beta)$ be the upward propagating intensity incident on the surface with $I_{in}(\beta) = 0$ for all $\beta > nk_o$. The output intensity, $I_{out}(\beta')$, is the incoherent sum of all input intensities which scatter into the direction β' weighted by the coupling strength. Given that $S(G) = S(\beta' - \beta)$ is the coupling strength between input β and output β' , we can write

$$I_{out}(\beta') = \int_{\mathbb{R}^2} I(\beta) S(\beta' - \beta) d^2\beta, \quad (4)$$

which is a convolution-type integral that can conveniently be calculated via Fourier transforms. Next we normalize and azimuthally average I_{out} ,

$$I_{out}(\beta') = \frac{1/(2\pi) \int_0^{2\pi} I_{out}(\beta') d\phi}{\int_0^{2\pi} \int_0^{k_o} I_{out}(\beta') \beta' d\phi d\beta'} \quad (5)$$

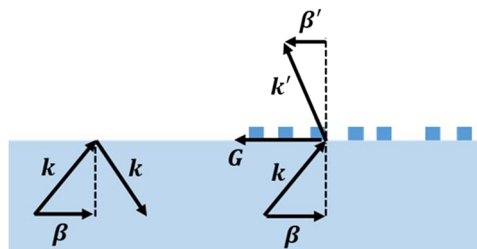


FIG. 2. Vector geometry used for analytical model. Plane waves with wave vector k are incident on a high-to-low index interface. A wave that would normally have TIR at a flat interface (left) can interact with the lattice momentum G to scatter into free space (right).

We then calculate a normalized directional enhancement by comparing $I_{out}(\beta')$ with a reference,

$$\gamma_{dn}(\beta') = \frac{I_{out}(\beta')}{I_{ref}(\beta')}.$$
 (6)

This metric describes the change in the emission profile shape from the reference profile (e.g., Lambertian emission) to the output profile (e.g., emission profile from a patterned surface) and is decoupled from the total change in power between the two. LED emission is typically well approximated by a Lambertian intensity profile in which case the observed intensity falls as the cosine of the observation angle. It is found after a coordinate transformation from angle space to k-space that

$$I_{lam}(\beta') = I_o,$$
 (7)

with I_o being constant. Alternatively, for an isotropic emitter embedded in the active medium, as is the case in our FDTD simulations, the emitted intensity is given by Eq. (8), which has higher intensity at the boundary of the light cone than at the center,

$$I_{iso}(\beta') \propto \frac{1}{\sqrt{k_o^2 n^2 - \beta'^2}}.$$
 (8)

Figure 3(a) shows the available parameter space of γ_{dn} as a function of β' and the pattern geometry scaling $\lambda/\langle r \rangle$ with fixed $D/\langle r \rangle = 0.7$, $n = 1.8$, and Lambertian radiance for both the input and reference. In the limits of large and small geometry scaling, we see that γ_{dn} approaches unity at all angles, i.e., there is no directional enhancement in these limits. In the transition from small to large geometry

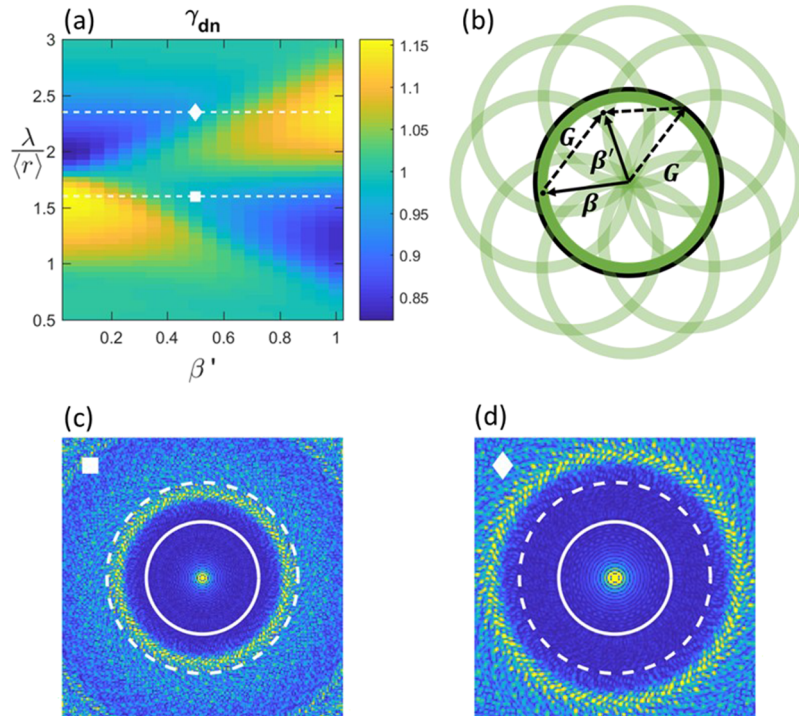


FIG. 3. (a) Parameter space of γ_{dn} . Values above one indicate enhanced directional emission in the output direction β' . (b) illustrates the principle of light scattering from an isotropic k-space structure to enhance directional emission. The dark green ring is a set of wave vectors propagating in the high index medium with approximately the same elevation angle, and the black ring represents the dominant feature of $S(G)$. Each of the light green rings is the set of input vectors scattered by a single array momentum vector G ; notice that these rings strongly overlap near the center but minimally overlap the edge, leading to enhanced forward emission. The vectors indicate how a single incident wave vector β phase matches with a moment vector G to produce a scattered vector β' which is nearer to the center of the light cone. (c) and (d) show $S(G)$ for the extreme cases of enhanced forward scattering and high angle scattering, respectively. White solid circle indicates the boundary of the free space light cone. White dashed circle indicates boundary of the high-index light cone with $n = 1.82$.

scaling, we see a peak appearing in the forward direction ($\beta' = 0$) then shifting to large angles ($\beta' = 1$). Figures 3(c) and 3(d) show $S(\mathbf{G})$ in color as well as the free space (white solid) and high-index (white dash) light cones for these two extreme cases.

To better understand the parameter space, we first note that for both the isotropic and Lambertian inputs, the largest k-space intensity annulus with differential width $d\beta$, which carries the most optical power, is located at the edge of the high-index light cone. This annulus is depicted as a dark green ring in Fig. 3(b). The thin black ring represents $S(\mathbf{G})$. The incident light is shifted (scattered) by each array momentum vector \mathbf{G} , yielding the light green rings. The light green rings represent a small set of shifted wave vectors. In fact there is a continuum of rings since $S(\mathbf{G})$ is a continuous function. Since $S(\mathbf{G})$ nearly overlaps with the incident wave vectors, all of the light green rings strongly overlap at $\beta' = 0$ and minimally overlap at $\beta' = k_o$, resulting in directional enhancement in the forward direction. This is the case shown in Fig. 3(c). Alternatively, Fig. 3(d) is the case where the edge of the high-index light cone is scattered to the edge of the free space light cone, therefore enhancing the high angle emission. Figure 3 also illustrates clearly the benefits of using aperiodic arrays with isotropic k-space. For each point of $S(\mathbf{G})$, there is a light green ring which represents light scattered into free space. For patterns with isotropic k-space, there is a much higher density of light green rings than, for example, in a structure with discrete Bragg peaks (i.e., periodic or quasi-periodic), thus leading to higher extraction efficiency.

It is apparent from this intuitive understanding that maximum directional enhancement for any particle array will occur when the dominant feature of the array's momentum space is present just inside the edge of the high-index light cone. Arrays such as the GA Vogel spiral, which have narrow, isotropic, and bright k-space features that can be controlled deterministically by the patterns' geometry are therefore ideal candidates for enhancing directional emission. The analytical parameter space and the FDTD simulation results provide guidance for the fabrication of GA Vogel spiral arrays with optimal extraction enhancement and directional emission enhancement. The fabrication of these devices is discussed in detail in Sec. IV.

IV. FABRICATION

Recently, various types of ceramic phosphors, in particular YAG:Ce³⁺, have been developed to produce white-light emitting LEDs.^{39,40} These ceramics typically sit on top of a layer of blue emitting LEDs and down convert the blue light to a white-light spectrum. This conversion method for white light production is more efficient than mixing multiple LEDs of various colors to produce the desired spectrum.^{30,41} YAG:Ce³⁺ samples with measured index of refraction $n = 1.82$ were used as the active LED material in this work.

Forming particle arrays onto YAG:Ce³⁺ substrates is difficult with standard reactive ion etching processes due to its thermal and chemical stability. A viable alternative is to deposit a thin film of a different material onto the substrate to form the particle array from. TiO₂ is a popular material for forming photonic crystals on phosphor plates as it can be deposited over large areas and with relatively low-cost processes.^{40,42,43}

We fabricated a variety of TiO₂ nanodisk arrays on top of the YAG:Ce³⁺ substrates. For each array, the disk centers were arranged in a GA spiral array with an overall footprint of 100 μm , large enough that aperture diffraction effects could be ignored. The mean nearest neighbor separation $\langle r \rangle$ and disk diameter D was varied from pattern to pattern so that the effect of geometry scaling could be systematically studied. Figure 4(a) outlines the process flow for the fabrication which is here described in detail.

TiO₂ thin films were prepared on pre-cleaned YAG substrates by DC magnetron sputtering [see Fig. 4(b) for thin-film dispersion data]. A 3" diameter TiO₂ target with 99.998% purity from Kurt J Lesker was used with 10 cm separation between target and substrate and 240 W of dc power. The substrate was rotated at a constant 5 rpm to yield a homogeneous thin film. The atmosphere consisted of 2 parts argon and 1 part O₂ at 2.5 mTorr. Substrates were solvent cleaned after sputtering. To fabricate arrays of TiO₂ disks, PMMA A3 was spun on the thin film and disk array patterns were written with electron beam lithography (Zeiss Supra 40) with a dose of 200 $\mu\text{m C/cm}^2$ at a current of 36 pA. The sample was then developed in IPA:IMBK (3:1) for 2 min followed by the deposition

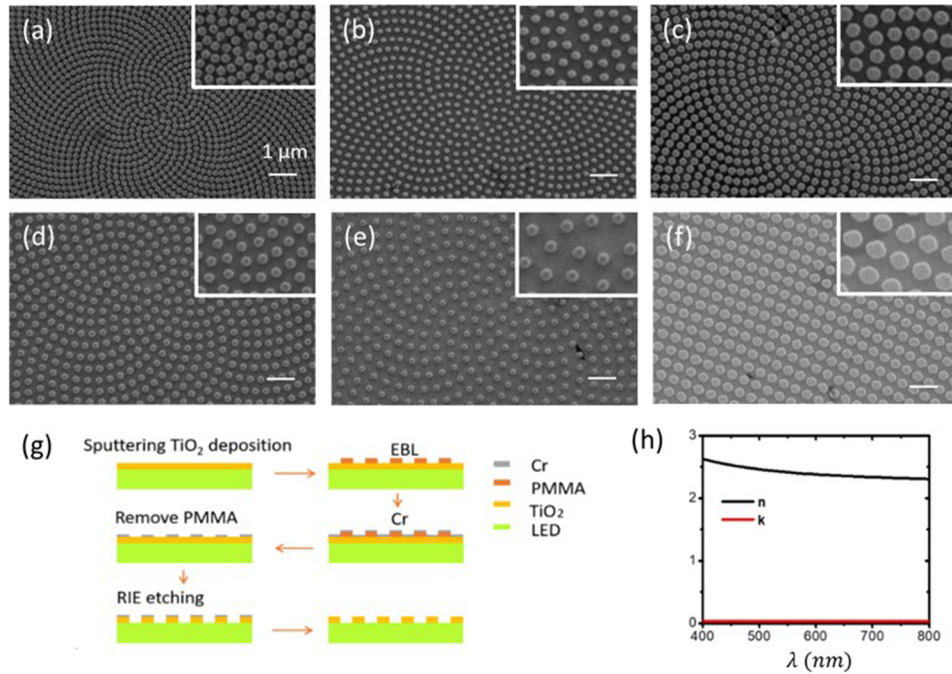


FIG. 4. (a) Process flow for GA Vogel spiral array nanodisk writing. (b) Dispersion data for TiO₂ thin film. [(c)–(h)] SEM images of TiO₂ nanodisks on YAG:Ce³⁺ substrates with mean separation of $\langle r \rangle = (220, 300, 320, 380, 450, 450)$ nm and pillar diameters of $D = (170, 190, 250, 230, 350)$ nm, respectively. White bar in lower right indicates 1 μm , and the insets show 2 \times enlargements.

of a 30 nm chromium mask using electron beam evaporation. After lifting off with remover 1165 and acetone, the disk array patterns were transferred to the YAG:Ce³⁺ substrate by plasma etching (RIE, Plasma-Therm, model 790) in a mixture of argon and SF6. Finally, the chromium mask was removed by wet etching in Transene 1020, leaving only TiO₂ pillars atop the YAG:Ce³⁺ substrate. Scanning electron microscope (SEM) images of several of the final GA Vogel arrays are shown in Figs. 4(c)–4(h). Measurements of the extraction enhancement and emission profiles are shown in Sec. V.

V. MEASUREMENTS

Angular emission profiles and PL spectra were concurrently measured using the optical setup shown Fig. 5(a). The sample was pumped with a 405 nm steady-state laser, and emission was collected with a 100 \times , 0.8 NA microscope objective (Olympus LMLFLN 100 \times BD). An iris placed at the intermediate image plane was used to control the light collection area, and a narrow band filter rejects any remaining pump light. Next, a fraction of the light is diverted with a beam cube splitter to measure the PL spectra (Ocean Optics QE65000). Finally, the last lens performs the optical Fourier transform of the emission surface onto a CCD camera (Evolution VF) to measure the k-space emission profile. Figures 5(b) and 5(c) show representative k-space and PL spectral measurements, respectively. This method measures the entire angular emission profile up to an objective-limited 54° in a single snapshot by mapping light emitted in the direction (θ, ϕ) to a pixel position.³⁴ The pixel position (i, j) corresponds to a transverse k-space value, (k_x, k_y), where $k_x = k_o \sin(\theta) \cos(\phi)$ and $k_y = k_o \sin(\theta) \sin(\phi)$ are the projected coordinates of the wave vector pointing in the direction (θ, ϕ) onto the plane. This method for measuring angular emission is much faster, simpler, and less prone to error than more traditional methods where a single photodetector is rotated about the sample on a long arm. The k-space values of each pixel are calibrated by placing a transmission grating with known spatial period into the sample position. With this procedure, we measured a value of $\Delta k_x/k_o = \Delta k_y/k_o = 0.0052$ per pixel.

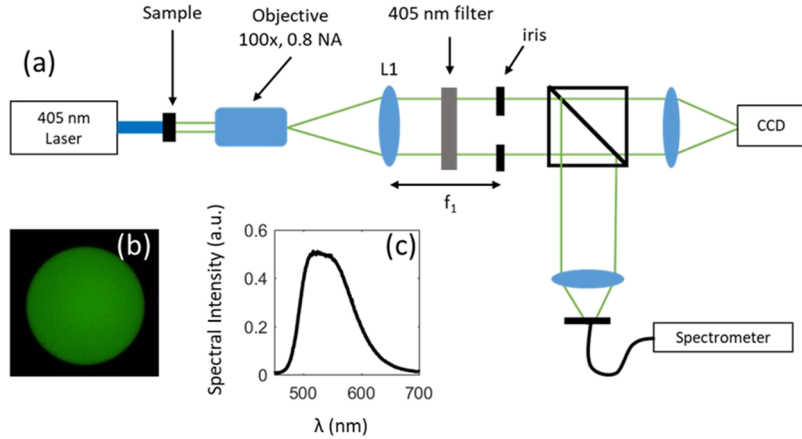


FIG. 5. (a) The optical setup for measuring k-space emission profile and PL spectra. Green lines trace out a plane wave emitted along the optical axis. (b) and (c) are representative k-space image and PL spectra, respectively.

Figure 6 shows a number of theoretical and measured k-space images. Each column represents a particular set of geometrical parameters of the particles as described in the caption. The top row is the simulated output intensity as described in Sec. III. For the input intensity, we used a Lambertian profile, as most LEDs exhibit Lambertian or near-Lambertian emission profiles.⁴⁴ In the middle row are measurements from patterned regions of the sample, and in the bottom row are measurements from nearby unpatterned sections of the sample (hereto referred to as “background” images). Note that the background images are consistent from one to another and show higher intensity at high angles than at the center. This is indicative of isotropic emission within the bulk which yields a radiant intensity given by Eq. (8). The measured emission profiles are clearly dependent on the geometry scaling of the pattern. Specifically, for both the simulated and measured profiles, increasing the mean pillar separation from 220 nm to 450 nm causes a shift in the intensity distribution from high angle concentration to forward concentration.

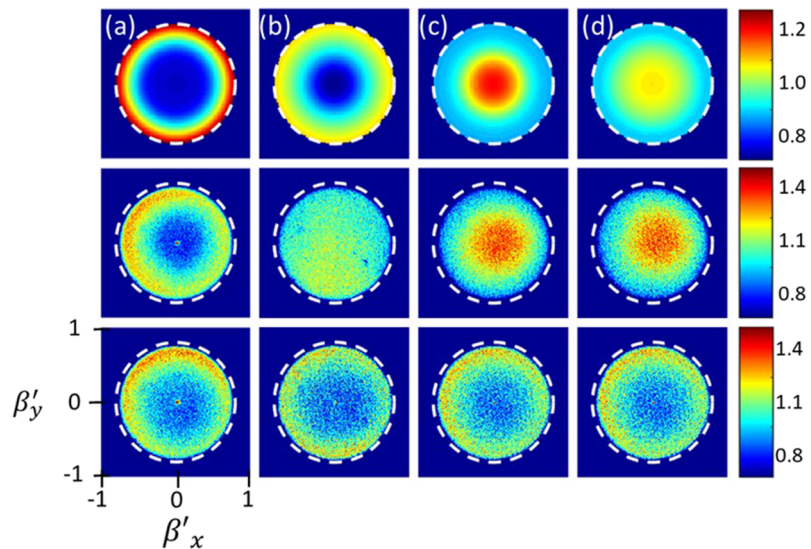


FIG. 6. k-space intensity profiles. Top row is analytical simulations assuming a Lambertian profile incident on the scattering array, middle row is measured data from patterned area, and bottom row is measured data from unpatterned area nearby above patterned area. Each color bar corresponds to all images in its respective row. Columns (a)–(d) are different spiral geometries with mean separation $\langle r \rangle = (220, 300, 380, 450)$ nm, respectively.

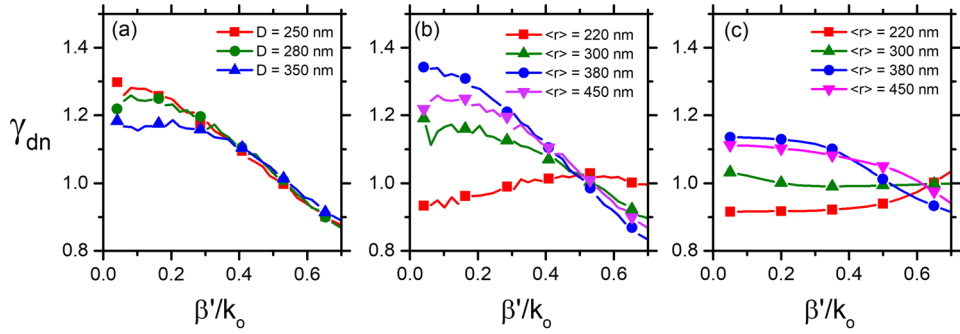


FIG. 7. Normalized directional enhancement plots. (a) shows negligible change in γ_{dn} with varying pillar diameter, D , and fixed mean separation $\langle r \rangle = 450$ nm. (b) shows γ_{dn} has significant sensitivity to $\langle r \rangle$, with increasing directional enhancement up to 35% in the forward direction as $\langle r \rangle$ increases from 220 nm to 450 nm. (c) modeled directional enhancement taken from appropriate horizontal slices of Fig. 3. The trend with changing $\langle r \rangle$ is in good agreement with measurements in (b).

To quantify the directional enhancement, the intensity profiles are first normalized by the total power, then the azimuthally averaged normalized intensity, $I_n(\beta')$, is calculated. Finally, the mean normalized intensity from the patterned region is divided by that of the background to yield the normalized directional enhancement, γ_{dn} . This is the same procedure used on modeled data as described in Sec. III. Figures 7(a) and 7(b) show γ_{dn} with varying D and $\langle r \rangle$. We observe that γ_{dn} is relatively insensitive to the pillar diameter, with only a slight dip in the forward enhancement ($\beta' = 0$) as the pillar size approaches the mean separation. On the other hand, it is quite sensitive to $\langle r \rangle$. Specifically, at $\langle r \rangle = 220$ nm, there is a slight drop in forward scattering and increase in high angle emission, and as $\langle r \rangle$ is increased from 220 nm to 450 nm, we measure an increase in the forward enhancement up to 35%. These results are qualitatively in agreement with the modeled predictions shown in Fig. 7(c), which are the appropriate horizontal cuts of Fig. 3 assuming $\lambda = 550$ nm.

Measured PL spectra and extraction enhancement are shown in Figs. 8(a) and 8(b), respectively. Enhancement was measured by dividing background spectra into patterned spectra, and varied between 1.4 and 2.0. As $\langle r \rangle$ decreases, the maximum enhancement increases and the enhancement curve narrows although in all measured cases, the enhancement did not significantly vary over the majority of the emission band (500-600 nm). These measurements clearly demonstrate the capability of GA Vogel spiral arrays for enhancing light extraction and directional emission from active LED materials. Furthermore, general agreement between measurements with FDTD simulation (quantitatively and qualitatively) and modeling (qualitatively) shows a robust ability to predict the performance of scattering nanoparticle arrays atop active LED materials.

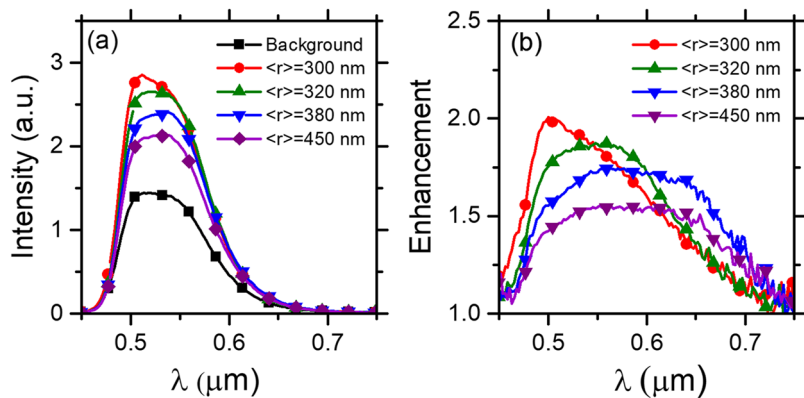


FIG. 8. (a) PL spectrum measurements with varying $\langle r \rangle$. Background is measured from an unpatterned surface near the patterned regions of the sample. (b) Extraction enhancement spectra calculated by dividing background into spectra from patterned surfaces. Line-styles between panels (a) and (b) correspond.

VI. CONCLUSION

In this work, we demonstrated the application of all-dielectric scattering nanoparticles in an aperiodic GA Vogel spiral array for the simultaneous enhancement of light extraction and directional emission from optically thick YAG:Ce³⁺ LED converter materials. We used full-vector numerical FDTD to find the optimal mean particle spacing and pillar height that maximize extraction enhancement. The optimal extraction enhancement is found to be 2.7× compared to a flat reference. We also developed an analytical model to understand and expediently optimize Vogel spiral array for directional enhancement of incoherent radiation. We patterned YAG:Ce³⁺ converters with TiO₂ nanodisks using the numerical and model results as guidance and measured peak extraction enhancement of 2× from patterned substrates compared to a flat reference using PL spectroscopy. We also measured power-normalized directional enhancement by using accurate Fourier-space emission spectroscopy and found a peak forward enhancement of 35%. Measurements were found in good agreement with numerical modeling predictions and in good qualitative agreement with the developed analytical model. Increasing the efficiency and controlling the direction of emission from LEDs are beneficial to a variety of LED applications. The extraction and directional enhancement capabilities of GA Vogel spiral array nanoparticles demonstrated within this work make them an attractive option for integration with commercially available LED active materials.

ACKNOWLEDGMENTS

We acknowledge the partial support of OSRAM Opto Semiconductors who contributed to this work by providing funding, the YAG:Ce³⁺ converter substrates, and valuable discussions regarding the integration with white-light LEDs. L.D.N. also wants to acknowledge the partial support of the NSF Grant No. ECCS-1643118 entitled Enhanced solar energy conversion by ultra-slow photon sub-diffusion in aperiodic media.

- ¹ N. Holonyak, *Am. J. Phys.* **68**, 864–866 (2000).
- ² N. F. Gardner, G. O. Miller, Y. C. Shen, G. Chen, S. Watanabe, W. Gtz, and M. R. Krames, *Appl. Phys. Lett.* **91**, 243506 (2007).
- ³ S. Nakamura, T. Mukai, and M. Senoh, *Appl. Phys. Lett.* **64**, 1687–1689 (1994).
- ⁴ V. Haerle, B. Hahn, S. Kaiser, A. Weimar, S. Bader, F. Eberhard, A. Plossl, and D. Eisert, *Phys. Status Solidi A* **201**, 2736–2739 (2004).
- ⁵ O. B. Shchekin, J. E. Epler, T. A. Trottier, T. Margalith, D. A. Steigerwald, M. O. Holcomb, P. S. Martin, and M. R. Krames, *Appl. Phys. Lett.* **89**, 071109 (2006).
- ⁶ A. Wilm, *Proc. SPIE* **7001**, 700101–70010F (2008).
- ⁷ H. Zhao, G. Liu, J. Zhang, R. A. Arif, and N. Tansu, *J. Disp. Technol.* **9**, 212–225 (2013).
- ⁸ P. Kivilahti, L. Riuttanen, J. Oksanen, S. Suihkonen, M. Ali, H. Lipsanen, and J. Tulkki, *Appl. Phys. Lett.* **101**, 021113 (2012).
- ⁹ C. Wiesmann, K. Bergenek, N. Linder, and U. Schwarz, *Laser Photonics Rev.* **3**, 262–286 (2009).
- ¹⁰ J. Y. Joo, C. S. Kang, S. S. Park, and S.-K. Lee, *Opt. Express* **17**, 23449–23458 (2009).
- ¹¹ J. Shakya, K. H. Kim, J. Y. Lin, and H. X. Jiang, *Appl. Phys. Lett.* **85**, 142–144 (2004).
- ¹² A. David, H. Benisty, and C. Weisbuch, *J. Disp. Technol.* **3**, 133–148 (2007).
- ¹³ A. David, T. Fujii, R. Sharma, K. McGroddy, S. Nakamura, S. P. DenBaars, E. L. Hu, C. Weisbuch, and H. Benisty, *Appl. Phys. Lett.* **88**, 061124 (2006).
- ¹⁴ C. Wiesmann, K. Bergenek, N. Linder, and U. Schwarz, *Proc. SPIE* **6989**, 69890L (2008).
- ¹⁵ H. Benisty, J. Danglot, A. Talneau, S. Enoch, J. M. Pottage, and A. David, *IEEE J. Quantum Electron.* **44**, 777–789 (2008).
- ¹⁶ M.-K. Kwon, J.-Y. Kim, I.-K. Park, K. S. Kim, G.-Y. Jung, S.-J. Park, J. W. Kim, and Y. C. Kim, *Appl. Phys. Lett.* **92**, 251110 (2008).
- ¹⁷ C.-F. Lai, J.-Y. Chi, H.-H. Yen, H.-C. Kuo, C.-H. Chao, H.-T. Hsueh, J.-F. T. Wang, C.-Y. Huang, and W.-Y. Yeh, *Appl. Phys. Lett.* **92**, 243118 (2008).
- ¹⁸ K. Bergenek, C. Wiesmann, R. Wirth, L. O’Faolain, N. Linder, K. Streubel, and T. F. Krauss, *Appl. Phys. Lett.* **93**, 041105 (2008).
- ¹⁹ K. McGroddy, A. David, E. Matioli, M. Iza, S. Nakamura, S. DenBaars, J. S. Speck, C. Weisbuch, and E. L. Hu, *Appl. Phys. Lett.* **93**, 103502 (2008).
- ²⁰ J. J. Wierer, Jr., A. David, and M. M. Megens, *Nat. Photonics* **3**, 163 (2009).
- ²¹ A. David, *J. Disp. Technol.* **9**, 301–316 (2013).
- ²² A. Lenef, J. F. Kelso, and A. Piquette, *Opt. Lett.* **39**, 3058–3061 (2014).
- ²³ R. Windisch, C. Rooman, S. Meinlschmidt, P. Kiesel, D. Zipperer, G. H. Dhler, B. Dutta, M. Kuijk, G. Borghs, and P. Heremans, *Appl. Phys. Lett.* **79**, 2315–2317 (2001).
- ²⁴ S. Illek, I. Pietzonka, A. Ploessl, P. Stauss, W. Wegleiter, R. Windisch, R. Wirth, H. Zull, and K. P. Streubel, *Proc. SPIE* **4996**, 18–25 (2003).

- ²⁵ A. David, T. Fujii, E. Matioli, R. Sharma, S. Nakamura, S. P. DenBaars, C. Weisbuch, and H. Benisty, *Appl. Phys. Lett.* **88**, 073510 (2006).
- ²⁶ N. Lawrence, J. Trevino, and L. Dal Negro, *J. Appl. Phys.* **111**, 113101 (2012).
- ²⁷ G. Ke, D. Mengqi, C. I. Osorio, and K. A. Femius, *Laser Photonics Rev.* **11**, 1600235 (2017).
- ²⁸ J. Trevino, H. Cao, and L. Dal Negro, *Nano Lett.* **11**, 2008–2016 (2011).
- ²⁹ L. Dal Negro, N. Lawrence, and J. Trevino, *Opt. Express* **20**, 18209–18223 (2012).
- ³⁰ H. Sun, A. Piquette, M. Raukas, and T. D. Moustakas, *IEEE Photonics J.* **8**, 1–10 (2016).
- ³¹ A. Oskooi, *Appl. Phys. Lett.* **106**, 041111 (2015).
- ³² L. Dal Negro, R. Wang, and F. A. Pinheiro, *Crystals* **6**, 161 (2016).
- ³³ N. Lawrence, J. Trevino, and L. Dal Negro, *Opt. Lett.* **37**, 5076–5078 (2012).
- ³⁴ N. Le Thomas, R. Houdré, M. V. Kotlyar, D. O'Brien, and T. F. Krauss, *J. Opt. Soc. Am. B* **24**, 2964–2971 (2007).
- ³⁵ X.-H. Li, R. Song, Y.-K. Ee, P. Kumorkaew, J. F. Gilchrist, and N. Tansu, *IEEE Photonics J.* **3**, 489–499 (2011).
- ³⁶ T. Wei, Q. Kong, J. Wang, J. Li, Y. Zeng, G. Wang, J. Li, Y. Liao, and F. Yi, *Opt. Express* **19**, 1065–1071 (2011).
- ³⁷ H. Jeong, D. J. Park, H. S. Lee, Y. H. Ko, J. S. Yu, S.-B. Choi, D.-S. Lee, E.-K. Suh, and M. S. Jeong, *Nanoscale* **6**, 4371–4378 (2014).
- ³⁸ S. Fan, P. R. Villeneuve, J. D. Joannopoulos, and E. F. Schubert, *Phys. Rev. Lett.* **78**, 3294–3297 (1997).
- ³⁹ S. Nishiura, S. Tanabe, K. Fujioka, and Y. Fujimoto, *Opt. Mater.* **33**, 688–691 (2011).
- ⁴⁰ A. Mao, C. D. Schaper, and R. F. Karlicek, Jr., *Nanotechnology* **24**, 085302 (2013).
- ⁴¹ M. Raukas, J. Kelso, Y. Zheng, K. Bergeneck, D. Eisert, A. Linkov, and F. Jermann, *ECS J. Solid State Sci. Technol.* **2**, R3168–R3176 (2013).
- ⁴² B. K. Park, H. K. Park, J. H. Oh, J. R. Oh, and Y. R. Do, *J. Electrochem. Soc.* **159**, J96–J106 (2012).
- ⁴³ J. R. Oh, Y. K. Lee, H. K. Park, and Y. R. Do, *J. Appl. Phys.* **105**, 043103 (2009).
- ⁴⁴ I. Moreno and C.-C. Sun, *Opt. Express* **16**, 1808–1819 (2008).